

# Analytical and numerical studies of periodic superradiance

Hideaki Hara,<sup>1,\*</sup> Yuki Miyamoto,<sup>1,†</sup> Junseok Han,<sup>1,2</sup> Riku Omoto,<sup>1</sup> Yasutaka Imai,<sup>1</sup>  
Akihiro Yoshimi,<sup>1</sup> Koji Yoshimura,<sup>1</sup> Motohiko Yoshimura,<sup>1</sup> and Noboru Sasao<sup>1,‡</sup>

<sup>1</sup>*Research Institute for Interdisciplinary Science, Okayama University, Okayama, 700-8530, Japan*

<sup>2</sup>*Department of Physics and Astronomy, Seoul National University, Seoul, Korea*

(Dated: December 4, 2024)

We conduct a theoretical study to understand the periodic superradiance observed in an Er:YSO crystal. First, we construct a model based on the Maxwell-Bloch equations for a reduced level system, a pair of superradiance states and a population reservoir state. We then derive two-variable equations consisting of the coherence and population difference between the two superradiance states, which contain the essential feature of the periodic superradiance. The two-variable equations clarify a mathematical structure of this periodic phenomenon and give analytical forms of the period, pulse duration, and number of emitted photons. Furthermore, analysis of the eigenvalues of the linearized differential equations shows that periodic superradiance can be realized only for certain parameters. Our model successfully reproduces the periodic behavior, but the actual experimental parameters are found to be outside the parameter region for the periodic superradiance. This result implies that some other mechanism(s) is required. As one example, assuming that the field decay rate varies with the electric field, the periodic superradiance can be reproduced even under the actual experimental condition.

## I. INTRODUCTION

Superradiance (SR), predicted by Dicke [1], is one of the coherent phenomena caused by cooperative spontaneous emission. Unlike ordinary spontaneous emission, a short intense optical pulse with a peak height proportional to  $N^2$ , where  $N$  is the number of atoms involved, is emitted due to the creation of a macroscopic dipole. For SR generation, this macroscopic dipole must develop within a decoherence time  $T_2$ . Many studies on SR have been carried out both theoretically and experimentally. So far SR has been observed in gases [2–4] and solid-state materials [5–9].

Recently, we have observed SR pulses with a quasiperiodic time structure in an Er:YSO crystal [10]. The periodic behavior persists during a continuous-wave (CW) laser excitation. We refer to this phenomenon as “periodic superradiance”. We provided a qualitative model to understand this periodicity, in which a cyclic process of a continuous supply of population inversion and a sudden burst of SR is repeated. The excitation power dependence measurements supported the validity of the model. However, our model was entirely qualitative and could not reproduce any observed SR quantities, such as period, pulse duration, and number of SR photons emitted.

SR is often described by the Maxwell-Bloch equations [11], which are nonlinear differential equations representing the dynamics of population, coherence, and radiation. For example, a single SR pulse can be obtained as a numerical or analytical solution of the Maxwell-Bloch equations for a fully excited two-level system. Because periodic SR has been observed only recently, there

have been no quantitative theoretical studies using the Maxwell-Bloch equations or other frameworks. A similar phenomenon, self-pulsing in laser media, is well known, where persistent pulses are generated under CW excitation. Numerous theoretical studies have addressed this phenomenon and successfully reproduced it using rate equations [12]. However, since coherence plays a central role in SR, such treatments cannot be directly applied to periodic SR.

In this paper, we report on more quantitative studies of the periodic SR than the model we constructed in Ref. [10]. First, we construct a model based on the Maxwell-Bloch equations for a reduced number of energy levels, a pair of SR states plus a population reservoir state. We find that the model, abbreviated as the extended two-level Maxwell-Bloch model (X2MB), can successfully generate periodic SR pulses under CW laser excitation. We then derive from the X2MB equations a pair of nonlinear differential equations of coherence and population difference, which are referred to as the truncated two-level Bloch model (T2B). We show that this simple two-variable equation contains the essential feature of periodic SR pulses. In fact, the characteristic quantities of SR, such as period, FWHM (full-width-half-maximum) pulse duration and number of emitted photons, can be expressed analytically by its integral. Another important result of the X2MB model is the classification of the parameter space into two separate regions; the periodic SR region and the other region. Only the periodic SR region exhibits periodic SRs. The classification is done by analyzing the eigenvalues of the linearized X2MB equations around the equilibrium points. We find that, somewhat unexpectedly, our experimental parameter set lies outside the periodic SR region. This result holds even when we allow the parameters to vary over a wide range of their uncertainties. We therefore conclude that some other mechanism(s) is required to reproduce the observed

\* hhara@okayama-u.ac.jp

† miyamo-y@cc.okayama-u.ac.jp

‡ sasao@okayama-u.ac.jp

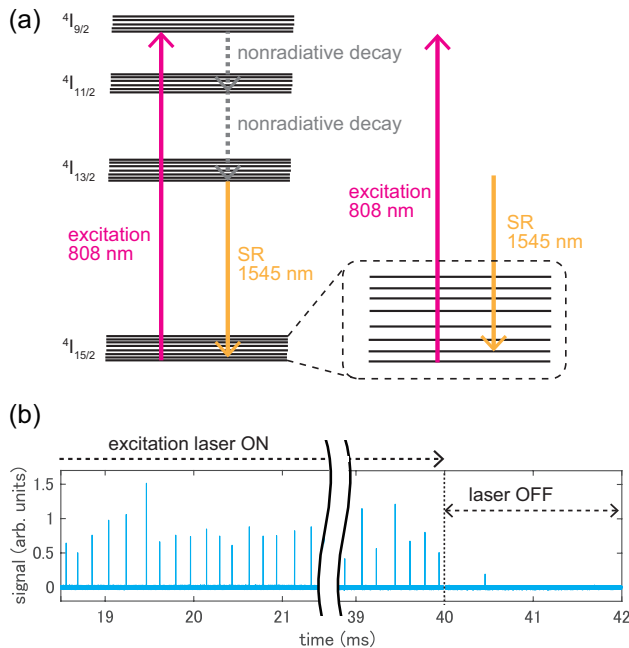


FIG. 1. (a) Energy diagram of an  $\text{Er}^{3+}$  ion doped in a YSO crystal. The dashed rounded square shows an enlarged view of the  ${}^4\text{I}_{15/2}$  ground state. (b) Example of the waveform of the observed periodic superradiance in the middle 3 ms of the excitation and from 1 ms before the excitation laser is turned off. The excitation laser is turned on for 40 ms from  $t = 0$ .

periodic SR. As an example of such mechanisms, we introduce a modulation of the field decay rate, *i.e.* the rate of electric field emission to the outside of the crystal. The X2MB model with this modification is found to give much more satisfactory results. We believe that the above studies explore intriguing aspects of the Maxwell-Bloch equations and shed new light on SR physics.

This paper is organized as follows. In Sec. II, a brief summary of our experimental results [10] is given. In Sec. III, the basic equations for our experimental system are introduced, and they are solved both analytically and numerically. The necessary condition for the periodic SR is also investigated. In Sec. IV, we discuss other possible mechanisms that cause the periodic behavior and modify the equations with a modulation of the field decay rate.

## II. SUMMARY OF EXPERIMENTAL RESULTS

First, we briefly summarize our experimental results [10]. The relevant energy diagram of  $\text{Er}^{3+}$  ions doped in a YSO crystal is shown in Fig. 1 (a). The crystal field splits each state into multiple Stark levels. An excitation laser at 808 nm pumps up  $\text{Er}^{3+}$  ions from the ground state to the lowest Stark level of the  ${}^4\text{I}_{9/2}$  state. After rapid decay via nonradiative processes, the population accumulates in the lowest Stark level of the  ${}^4\text{I}_{13/2}$  state with a long lifetime of about 10 ms. The SR pulses with

a wavelength of 1545 nm are generated in the transition between the two SR states, *i.e.* from the lowest Stark level of the  ${}^4\text{I}_{13/2}$  state to the second lowest Stark level of the  ${}^4\text{I}_{15/2}$  ground state.

The  $\text{Er}^{3+}$  ions at site 2, whose number density is about  $5 \times 10^{18} \text{ cm}^{-3}$ , are used in our experiment. The excitation laser diameter ( $2w_0$ ) is about  $300 \mu\text{m}$  and the input power is 90 mW. It propagates through the 6 mm long crystal. The excitation laser is turned on for 40 ms every 200 ms and the 40 ms excitation data are acquired repeatedly. The detailed setup and procedure are described in Ref. [10].

Under the above experimental scheme, we observed periodic SR pulses as shown in Fig. 1 (b). The pulses appear several ms after the excitation laser is turned on ( $t = 0$ ), and disappear right after it is turned off ( $t = 40$  ms), occasionally followed by one additional SR pulse. The mean period between SR pulses ( $T$ ) and the standard deviation determined by the Gaussian fit to the peak interval histogram are  $160 \mu\text{s}$  and  $20 \mu\text{s}$ , respectively. The mean FWHM pulse duration ( $\Delta T$ ) of SR and the standard deviation are  $20 \text{ ns}$  and  $5 \text{ ns}$ , respectively. The number of photons ( $N_{\text{SR}}$ ) in a single SR pulse is estimated to be  $\mathcal{O}(10^{12})$ . For future convenience, we summarize our main experimental results:

$$(T, \Delta T, N_{\text{SR}}) = (160 \mu\text{s}, 20 \text{ ns}, 10^{12}). \quad (1)$$

Note that in addition to the pulse-to-pulse fluctuations,  $(T, \Delta T, N_{\text{SR}})$  vary with experimental conditions such as the position of the excitation laser; therefore, they must be considered as representative values [10]. The periodic time structure can be understood qualitatively by a simple model, in which a cyclic process of a continuous supply of population inversion and a sudden burst of SR emission are repeated.

## III. EXTENDED TWO-LEVEL MODEL BASED ON THE MAXWELL-BLOCH EQUATIONS

In this section, we first construct a model based on the Maxwell-Bloch equations with reduced energy levels (Sec. III A). This model, which can only be solved by numerical integration, is the basis of all the results presented in this paper. We refer to this model as an extended two-level model based on the Maxwell-Bloch equations (X2MB model for short) for a reason explained below. We then present a much simpler model that reveals essential features of the periodic SR (T2B model) (Sec. III B). It is a set of nonlinear differential equations with only two variables, coherence and population difference between the two SR states. Analytical solutions of this simple two-variable model are shown to reproduce main features of the X2MB simulation results.

The X2MB model contains many physical parameters. We discuss how we determine the central value and uncertainty of these parameters (Sec. III C). They are used in the numerical simulations. We find that the periodic SR

occurs only in a certain restricted region of the parameter space. The conditions for the parameters necessary for the periodic SR to appear are clarified by analyzing linearized X2MB equations around equilibrium points (Sec. III D). We then perform numerical simulations with parameters both inside and outside of the “predicted” periodic SR region (Sec. III E). Finally we conclude this section by searching for a parameter set that reproduces our experimental results (Sec. III F).

### A. Extended two-level model: concept and basic equations

As described in the previous section, the actual process observed in our experiment involves many ionic states and transitions among them. It is virtually impossible to reproduce this complicated process quantum mechanically. Fortunately we find that the transitions may be classified into two broad categories: coherent transitions which require quantum treatments, and incoherent ones which can be described by rate equations. In our case, the transition between the SR states is coherent and needs to be treated by the Schrödinger (or Bloch) equation. All other transitions are incoherent. Note that the pumping process by a laser beam is in principle coherent, but the  $\text{Er}^{3+}$  ions pumped up by the laser decay rapidly by nonradiative processes and lose their phase memory before reaching the upper SR state. Thus, in fact, we may consider it an incoherent pumping process.

The above considerations leads to a highly simplified model of the process shown in Fig. 2. In the following, this model is explained in more detail using Fig. 2. The states  $|1\rangle$  and  $|2\rangle$  correspond to the lowest and the second lowest Stark levels of the  ${}^4\text{I}_{15/2}$  ground state, and  $|3\rangle$  corresponds to the lowest level of  ${}^4\text{I}_{13/2}$ , respectively. As mentioned above, coherence develops only between  $|3\rangle$  and  $|2\rangle$ , and generates SR pulses. This level system can be thought of as a Maxwell-Bloch system in the two levels between  $|3\rangle$  and  $|2\rangle$ , with the addition of  $|1\rangle$  as a reservoir. Hence the name “extended two-level model”. The excitation to the lowest Stark level of the  ${}^4\text{I}_{9/2}$  state and the subsequent nonradiative decay  $|3\rangle$  are combined and represented by a single pumping rate  $P_{13}$ . Among the deexcitation processes from  $|3\rangle$  to the various Stark levels of the  ${}^4\text{I}_{15/2}$  ground state, only a radiative decay rate  $A_{32}$  from  $|3\rangle$  to  $|2\rangle$  contributes to the SR. The deexcitation processes from  $|3\rangle$  to other than  $|2\rangle$  and the other incoherent processes between  $|3\rangle$  and  $|2\rangle$  are together represented as a deexcitation rate  $A_{31}$  from  $|3\rangle$  to  $|1\rangle$ . The population of the state  $|2\rangle$  decays to the state  $|1\rangle$  with a rate of  $A_{21}$ , which is dominated by nonradiative decays, making the development of macroscopic dipoles practically impossible.

We are now in a position to write Maxwell-Bloch type equations based on Fig. 2. After applying a rotating-wave approximation and a slowly varying envelope ap-

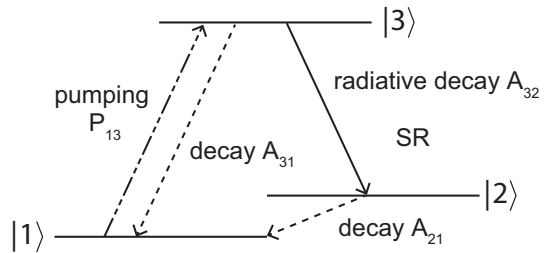


FIG. 2. Reduction to an extended two-level system in our model. The states  $|1\rangle$  and  $|2\rangle$  correspond to the lowest and the second lowest Stark levels of the  ${}^4\text{I}_{15/2}$  ground state, respectively. The state  $|3\rangle$  corresponds to the lowest Stark level of the  ${}^4\text{I}_{13/2}$  state. The solid arrow represents the coherent transition. The dashed arrows represent the incoherent decay. The double chain arrow represents the combination of the pumping (coherent process) and subsequent nonradiative decay (incoherent process).

proximation [11], we readily arrive at a set of equations (X2MB equations) shown below:

$$\frac{d\rho_{11}}{dt} = -P_{13}\rho_{11} + A_{31}\rho_{33} + A_{21}\rho_{22}, \quad (2)$$

$$\frac{d\rho_{22}}{dt} = \Omega_s\rho_{32} + A_{32}\rho_{33} - A_{21}\rho_{22}, \quad (3)$$

$$\frac{d\rho_{33}}{dt} = -\Omega_s\rho_{32} + P_{13}\rho_{11} - (A_{31} + A_{32})\rho_{33}, \quad (4)$$

$$\frac{d\rho_{32}}{dt} = \frac{\Omega_s}{2}(\rho_{33} - \rho_{22}) - \gamma_{32}\rho_{32}, \quad (5)$$

$$\frac{\partial\Omega_s}{\partial t} = -\kappa\Omega_s + \Omega_0^2\rho_{32} + \Omega_0^2R_{\text{sp}}\rho_{33}. \quad (6)$$

Here  $\rho_{ij}$  are the density matrix elements of states  $|i\rangle$  and  $|j\rangle$ . As shown in Eq. (2), the population change of  $|1\rangle$  is caused by the pumping and decay processes. The populations of  $|2\rangle$  and  $|3\rangle$  change with the SR generation in addition to the pumping and decay processes. The population changes due to the SR generation are represented by the first terms on the right-hand side of Eqs. (3) and (4). The Rabi frequency  $\Omega_s$  is defined as

$$\Omega_s \equiv i\frac{d_{32}E_0}{\hbar}, \quad (7)$$

where  $d_{32}$  is the transition dipole moment between  $|3\rangle$  and  $|2\rangle$ , and  $E_0$  is the slowly varying envelope of the electric field  $\vec{E}$  due to the SR radiation. In this study, without loss of generality, we set  $\Omega_s$  and  $\rho_{32}$  as real numbers. Equation (5) represents the time evolution of the coherence  $\rho_{32}$ , where  $\gamma_{32}$  is the decoherence rate. As mentioned above, we only consider the coherence between these states. Equation (6) is derived from the Maxwell electric field, and represents the time evolution of the SR electric field. Note that the differential operator  $\partial/\partial z$  in the Maxwell equation is replaced by  $1/L$ . This replacement is justified because the crystal length  $L$  is short

enough that the change in  $E_0$  can be neglected (homogeneous approximation). In this approximation, the emission of the SR electric field to the outside of the crystal is represented by the field decay rate  $\kappa(=c/n_0L)$ , where  $c$  and  $n_0$  are the speed of light and the refractive index of the crystal at a wavelength of SR, respectively. The second term in Eq. (6) represents the field development due to coherence, while the last term is a contribution to the SR electric field by spontaneous emissions. Although the rate  $R_{\text{sp}}$  is extremely small, it is necessary for the system to start the coherence development. In the following we will call  $R_{\text{sp}}$  the coherence trigger rate.

When analyzing/solving the X2MB model, it is convenient to introduce a frequency that characterizes the time scale of the system. This frequency, denoted by  $\Omega_0$ , is given by

$$\Omega_0 = \sqrt{\frac{N_0 d_{32}^2 \omega_{32}}{2\epsilon_0 \hbar}}, \quad (8)$$

where  $N_0$  is the number density of  $\text{Er}^{3+}$  ions at site 2 and  $\omega_{32}$  is the angular frequency between  $|3\rangle$  and  $|2\rangle$ . Another important observation is the hierarchy of time scales in the frequency parameters. In fact, the relationship among the magnitude of each rate,

$$\kappa \gg \gamma_{32}, A_{21} \gg P_{13}, A_{31}, A_{32} \gg R_{\text{sp}}, \quad (9)$$

is useful to understand the properties of our system. The field decay rate  $\kappa$ ,  $\mathcal{O}(10^{10})$  Hz, is the highest and dominates the time evolution of the system. The decoherence rate  $\gamma_{32}$ ,  $\mathcal{O}(10^{7\pm 1})$  Hz and the decay rate  $A_{21}$ ,  $\mathcal{O}(10^6)$  Hz, are much lower than the field decay rate, but are much higher than the other pumping and decay rates  $P_{13}$ ,  $A_{31}$ , and  $A_{32}$ ,  $\mathcal{O}(10^{1\pm 1})$  Hz. The coherence trigger rate  $R_{\text{sp}}$  is the smallest among the parameters: it does not play a significant role once it initiates the coherence development. The detailed values are given in Table I.

## B. Truncated two-level Bloch model

As mentioned in the introduction to this section, a much simpler model, the truncated two-level Bloch model (T2B model), can be derived from the X2MB equations. It has a much simpler structure than X2MB because it has only two variables, coherence and population difference. The T2B model is useful to shed light on essential features of the SR periodicity and will be discussed in more detail below.

To arrive at the T2B model, we first eliminate  $\rho_{11}$  using the relation  $\rho_{11} + \rho_{22} + \rho_{33} = 1$ . Second, the time derivative in Eq. (6) is ignored because the field decay rate  $\kappa$  is very high and dominates the time evolution of the system. This approximation makes the SR electric field directly proportional to the coherence  $\rho_{32}$ . Finally the tiny contribution of  $R_{\text{sp}}$  is also ignored. With these

approximations and after making Eqs. (2) - (6) dimensionless, the following differential equations are obtained:

$$\frac{dX}{d\tau} = XY, \quad (10)$$

$$\frac{dY}{d\tau} = -(X^2 - 1). \quad (11)$$

Here  $X$  is proportional to the coherence  $\rho_{32}$ , and thus to the SR electric field.  $Y$  is proportional to the deviation of  $\rho_{33} - \rho_{22}$  from the equilibrium point.  $\tau$  is the dimensionless time. In this paper, we refer to these equations as the T2B model. The derivation and definition of the variables are summarized in Appendix A.

Let us examine what the T2B model tells us. As is well known [13], the global feature is best analyzed by a streamline plot. Figure 3 (a) shows the streamlines of Eqs. (10)-(11). As can be seen, the stream flows clockwise and circles around the equilibrium point,  $(1,0)$ , in the  $XY$  plane, suggesting cyclic behavior. The line along which the solution  $(X, Y)$  moves depends on the initial value of  $(X, Y)$ . The cyclic motion in the  $XY$  plane corresponds to the periodic behavior.

Figure 3 (b) shows the numerical solution of the T2B model. The magenta solid and green dashed lines are  $X$  and  $Y$ , respectively. Since  $X$  is proportional to the SR electric field in our approximation, the magenta solid line indicates that the short optical pulses are generated periodically. The green dashed line indicates that the population inversion increases linearly due to the pumping and decay processes and that it drops rapidly due to the SR pulse generation. Figure 3 (c) is the extended view of Fig. 3 (b) around a single pulse. The magenta crosses are  $X$ . The blue line is the fit to  $X$  by a sech function, which is one of the characteristics of SR when coherence develops homogeneously over the target [14].

The analytical solution of the period  $T$  is obtained as follows. A simple manipulation of Eqs. (10) and (11) yields

$$YdY = \frac{1 - X^2}{X}dX. \quad (12)$$

Integrating Eq. (12), we obtain

$$Y^2 = C - (X^2 - \log(X^2)), \quad (13)$$

where the integration constant  $C$  has the relationship  $C = \log(e^{X_{\text{max},\text{min}}^2}/X_{\text{max},\text{min}}^2) = 1 + Y_{\text{max},\text{min}}^2$  with the maximum and minimum values of  $X$  and  $Y$ . After eliminating  $Y$  using Eq. (13), Eq. (10) becomes

$$d\tau = \left\{ X \sqrt{C - \log(e^{X^2}/X^2)} \right\}^{-1} dX. \quad (14)$$

Integrating Eq. (14) along the streamline from  $X_{\text{min}}$  to  $X_{\text{max}}$ , the period  $T$  is obtained as follows.

$$T = \int_{w_{\text{min}}}^{w_{\text{max}}} dw \left\{ w \sqrt{C - \log(e^w/w)} \right\}^{-1}, \quad (15)$$

$$w_{\text{min}} = -W_0(-e^{-C}), \quad w_{\text{max}} = -W_{-1}(-e^{-C}), \quad (16)$$

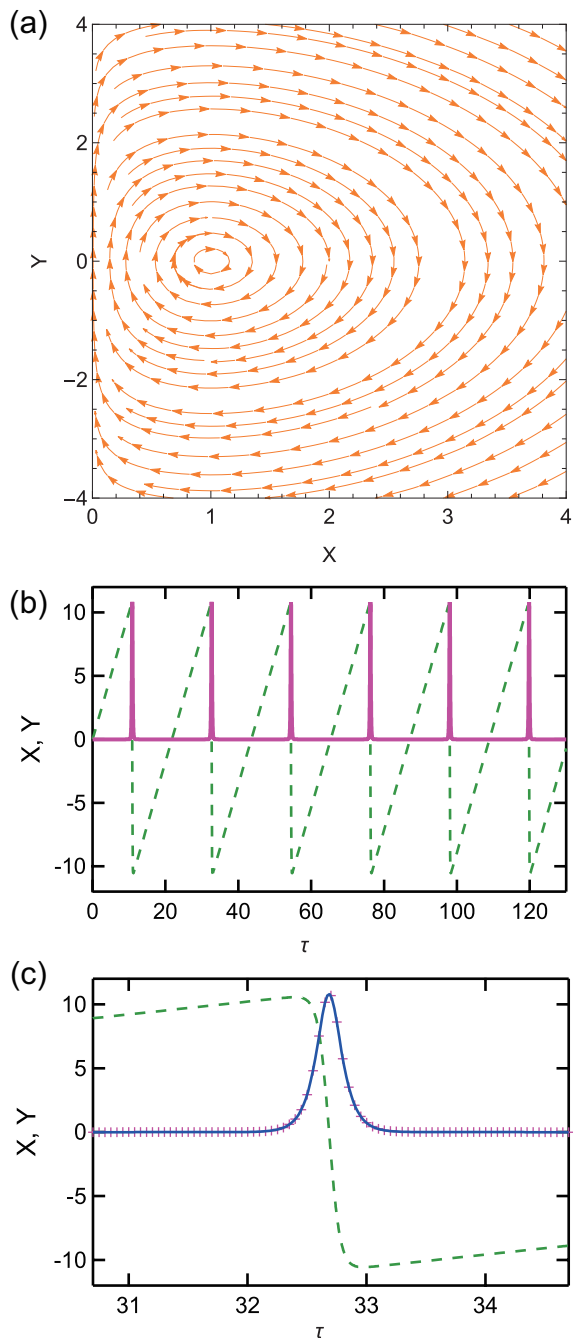


FIG. 3. (a) Streamline of Eqs. (10) and (11) in the  $XY$ -plane. (b) Solution of the T2B model. The magenta solid line is  $X$ , which is proportional to the SR electric field. The green dashed line is  $Y$ , which is proportional to the deviation of the population inversion from the equilibrium point. The minimum coherence required to find  $C$  is assumed to be  $\mathcal{O}(10^{-29})$ . (c) Extended view of (b) around a single pulse. The magenta crosses are  $X$ . The blue line is the fit to  $X$  by a sech function. The green dashed line is  $Y$ .

where  $w = X^2$  and  $W_J$  is the Lambert  $W$  function with branch index  $J$ .

Similarly, the half of the FWHM pulse duration  $\Delta T/2$  is obtained by integrating Eq. (14) along the streamline from  $X_{\max}/\sqrt{2}$  to  $X_{\max}$ , recalling that  $X$  is proportional to the SR electric field. The FWHM pulse duration  $\Delta T$  is given by

$$\Delta T = \int_{w_{\max}/2}^{w_{\max}} dw \left\{ w \sqrt{C - \log(e^w/w)} \right\}^{-1}. \quad (17)$$

By the way, by expanding  $W_J(x)$  in series of  $x$  or  $\log(-x)$  [15], we can derive approximate formulae for  $T$  and  $\Delta T$  when  $C \gg 1$ :  $T \simeq (2/\sqrt{C}) \log 2\sqrt{C} + 2\sqrt{C}$  and  $\Delta T \simeq 1.76/\sqrt{C}$ .

The number of photons emitted in a single SR pulse is estimated as  $Y_{\max} - Y_{\min}$  multiplied by an appropriate factor, since the sudden drop in the population difference in Fig. 3 (b) is caused by the SR generation.

The T2B model succeeds in capturing the essential features of SR periodicity. First, the periodic pulses can be reproduced by the T2B model. Second, the T2B model can also reproduce the temporal shape of the electric field of the sech function, which is characteristic of SR. Furthermore, the period, the FWHM pulse duration, and the number of photons emitted are expressed analytically with a single integration constant  $C$ . Unfortunately, it is not yet possible to derive  $C$  from a given set of parameters.

Finally, the validity of the analytical solution of the T2B model is mentioned. Only a summary is given here, see Appendix B for more details. We compare the analytical solution of the T2B model and the numerical simulation result of the X2MB model for the same parameter set. The period, the FWHM pulse duration, and the number of emitted photons are in good agreement. This result shows the validity of the T2B model derived using several approximations.

### C. Experimental parameters

In the following part, we consider the condition for the periodic SR and perform the numerical simulation for the different experimental parameter sets. Before that, we introduce the experimental parameters. The parameters in our experiment are shown in Table I. The upper part consists of the input parameters necessary to solve the X2MB equations. Only these parameters will be discussed in detail here. The pumping rate  $P_{13}$  is estimated from the approximately 85 % absorption of the 90 mW excitation laser. The radiative decay rate  $A_{32}$  is estimated from the fluorescence spectrum [18] and the absorption spectrum measured in our system. The decay rate  $A_{31}$  is estimated by subtracting  $A_{32}$  from the decay rate determined by the fluorescence lifetime of  $|3\rangle$  ( $9.20 \pm 0.02$  ms [18]). The decay rate  $A_{21}$  is measured by the time constant of the change in absorption from the lower state of SR to the third lowest Stark level of the  $^4I_{9/2}$  state [10]. The decoherence rate  $\gamma_{32}$  is estimated

TABLE I. Experimental parameters. The upper part consists of the input parameters to the X2MB equations. The middle part shows the parameters calculated by others. The bottom part is related to the crystal property, energy level, and laser. The measure of uncertainty of each parameter is also displayed. Here, the uncertainty does not mean  $1\sigma$ , but is only a guide. “factor  $U$ ” represents the uncertainty from factor  $1/U$  to  $U$ .

symbol	description	central value	measure of uncertainty	remark
$P_{13}$	pumping rate	200 Hz <sup>a</sup>	$\pm 100$	
$A_{32}$	radiative decay rate	4 Hz <sup>a</sup>	factor $10^b$	
$A_{31}$	decay rate	100 Hz <sup>a</sup>	$70 \leq A_{31} \leq 110$	
$A_{21}$	decay rate	$2.5 \times 10^6$ Hz	factor 3	Ref. [10]
$\gamma_{32}$	decoherence rate	$10^7$ Hz <sup>a</sup>	factor $10^a$	
$R_{\text{sp}}$	coherence trigger rate	$10^{-30}$ Hz <sup>a</sup>	see main text	
$\kappa$	field decay rate	$2.8 \times 10^{10}$ Hz	factor $3^c$	$c/n_0L$
$d_{32}$	transition dipole moment	$2.3 \times 10^{-32}$ C m	factor 3	$\sqrt{\frac{3\pi\epsilon_0\hbar c^3 A_{32}}{\omega_{32}^3}}$
$\Omega_0$	characteristic frequency of SR	$4.0 \times 10^{10}$ rad/s	factor 10	$\sqrt{\frac{N_0 d_{32}^2 \omega_{32}}{2\epsilon_0 \hbar}}$
$N_0$	number density of Er <sup>3+</sup> ions at site 2	$4.7 \times 10^{18}$ cm <sup>-3</sup>	factor $10^d$	0.1 % concentration
$N_{\text{Er}}$	total number of Er <sup>3+</sup> ions at site 2	$2.0 \times 10^{15}$	factor 10	$N_0 \pi w_0^2 L$
$n_0$	refractive index	1.8	$\pm 0.1$	Ref. [16, 17] <sup>e</sup>
$L$	crystal length	6 mm	negligible	
$w_0$	excitation laser radius	150 $\mu\text{m}$	$\pm 10$	
$\omega_{32}$	angular frequency	$1.2 \times 10^{15}$ rad/s	negligible	Ref. [18]

<sup>a</sup> Discussed in the main text.

<sup>b</sup> This uncertainty is mainly due to the uncertainty in  $N_0$ .

<sup>c</sup> The uncertainty determined from the crystal length is small, but the actual uncertainty should be large.

<sup>d</sup> The uncertainty determined from the concentration of the preparation is small, but the actual uncertainty is large due to the inhomogeneity of the crystal.

<sup>e</sup> The value of the refractive index at room temperature is estimated using the Sellmeier equation [16]. Applied from the microwave case [17], the refractive index is only a few percent different between 4 K and room temperature.

from the fact that the decoherence time should be longer than the duration of the SR pulses ( $\mathcal{O}(10)$  ns) and shorter than twice the lifetime of the lower state of SR ( $2 \times 400$  ns). In principle, the coherence trigger rate  $R_{\text{sp}}$  may be estimated by considering the spontaneous emission rate, its phase variation, and the modes of SR emission. In practice, however, it is difficult to estimate accurately because of its random nature. Fortunately, the final result is insensitive to this parameter. For example, even if it differs by ten orders of magnitude, the result such as period, FWHM pulse duration, and SR photon number will differ by a factor of less than 2. We arbitrarily assume a very small value in this paper;  $R_{\text{sp}} = 10^{-30}$ .

A few comments are in order here. First, we note that most of the parameters are not accurately determined. We give rough estimates of their uncertainties in Table I and in its footnotes, along with their central values. Second, given the rather large parameter uncertainties, we varied them widely in the simulation to study their dependence. We find that our conclusion is essentially unchanged, as shown below.

#### D. Conditions for periodic SR

Given a set of parameters, it is desirable to know whether or not the X2MB equations produce periodic SRs. Since it is impossible to run a simulation for every parameter set, such predictability is essential to draw the conclusion of this section. To this end, we linearize the X2MB equations around equilibrium points, and analyze the eigenvalues of the resulting Jacobi matrix. We classify the parameter space based on the sign of the eigenvalues and exclude the region where periodic SR cannot occur. This analysis is elaborated below.

##### 1. Linearized X2MB equations and Jacobi matrix

We first rewrite the original X2MB equations, Eqs. (2) - (6), into dimensionless forms. This is done in Appendix A to obtain Eqs. (A9) - (A12). We then expand them around the equilibrium points given by Eqs. (A17) - (A20). The final form of the linearized equations is

$$\frac{d\vec{y}}{dt} = J\vec{y}, \quad J = \begin{pmatrix} -b_{00} & 1 & 0 & 0 \\ u_2^e & -b_{11} & u_0^e & 0 \\ -u_1^e & -u_0^e & b_{22} & b_{23} \\ 0 & 0 & b_{32} & b_{33} \end{pmatrix}, \quad (18)$$

where  $J$  is a Jacobi matrix and  $y_i \equiv u_i - u_i^e$  ( $i = 0, 1, 2, 3$ ) is a deviation from the equilibrium point. The solution of Eq. (18) can be expressed as  $\vec{y} = \sum_{i=0}^3 C_i \vec{x}_i \exp(\lambda_i t)$  using the eigenvalues  $\lambda_i$  of  $J$ , the eigenvectors  $\vec{x}_i$  for each eigenvalue, and the constants  $C_i$ . As noted above, the behavior around the equilibrium point is determined by the eigenvalues of the Jacobi matrix. For example, if the real parts of the eigenvalues are all negative, then the system approaches the equilibrium point ( $\vec{y} \rightarrow \vec{0}$ ). In other words, the periodic SR generation requires the system to be outside such a region. In fact, there are two equilibrium solutions to the X2MB equations. One is the “trivial solution” with zero electric field, and the other is the “nontrivial solution” with finite electric field. For periodic SR, the system is expected to move away from the equilibrium point of the nontrivial solution. Thus, the system should be in the region where at least one real part of the eigenvalues is positive for the nontrivial equilibrium point. This is a necessary condition, but it may not be sufficient. It does not hold in principle, but has been investigated under several conditions and found to be correct. Our expectation is confirmed by the numerical simulation results. We refer to the above region, where the periodic SR is expected to occur, as the “periodic SR region”.

## 2. Plot of the periodic SR region

As pointed out in Sec.III C, there are five important parameters in our model;  $P_{13}$ ,  $A_{31}$ ,  $A_{32}$ ,  $A_{21}$ , and  $\gamma_{32}$ . Among them, only  $P_{13}$  is controllable by the experiment. Nevertheless, we have varied all these parameters to study the parameter dependence of the periodic SR region. For easier understanding, only  $(A_{21}, P_{13})$  are treated as variables at first, while the other parameters are fixed at certain values. Then all other parameters are varied one by one, as is discussed below.

Figure 4 shows the periodic SR regions in the  $(A_{21}, P_{13})$  plane for different  $A_{32}$  with  $(A_{31}, \gamma_{32})$  fixed at  $(10^2, 10^7)$  Hz. Here, and below, the underline below the numerical value indicates that it corresponds to the actual experimental value shown in Table I. The blue dotted, green solid, black dashed, and red dot-dashed lines are the boundaries of the periodic SR regions for  $A_{32} = 2, \underline{4}, 15,$  and  $100$  Hz, respectively. The periodic SR regions within these boundaries are colored. The green region corresponds to the case with the actual value of  $(A_{31}, A_{32}, \gamma_{32})$ , but not of  $(A_{21}, P_{13})$ . When  $A_{32}$  is varied to the higher frequency, the diagonal line (DL) shifts to the lower right. The vertical line (VL) shifts to the lower frequency side for  $A_{32} < 15$  Hz, and it shifts to the higher frequency side for  $A_{32} > 15$  Hz. We also examine how the results change when the other parameters,  $\gamma_{32}$  and  $A_{31}$ , are varied. If  $\gamma_{32}$  is changed from 0 to  $10^8$  Hz with  $(A_{31}, A_{32}) = (10^2, \underline{4})$  Hz, the results are almost the same as the green region. If  $A_{31}$  is changed from  $10^2$  Hz to  $10$  or  $10^3$  Hz with  $(\gamma_{32}, A_{32}) = (10^7, \underline{4})$  Hz, the vertical line

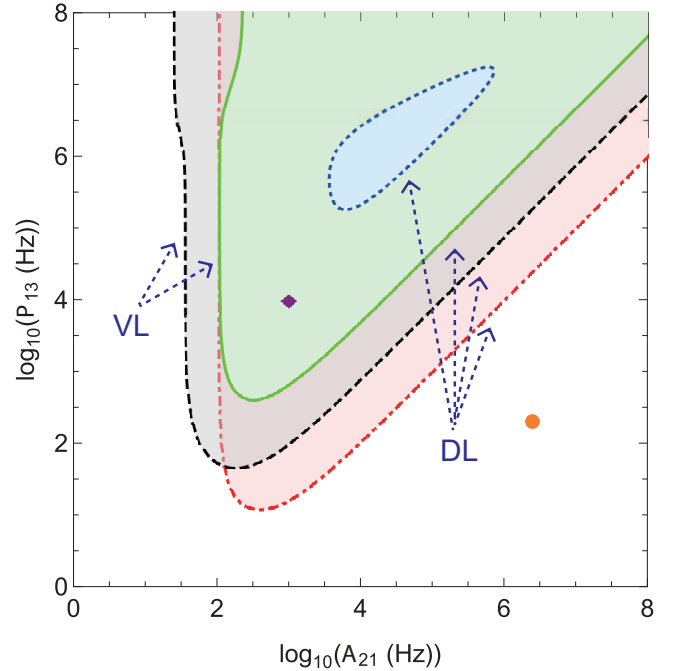


FIG. 4. Periodic SR regions in the  $(A_{21}, P_{13})$  plane for different  $A_{32}$  with  $(A_{31}, \gamma_{32})$  fixed at  $(10^2, 10^7)$  Hz. The periodic SR regions are colored. The blue dotted, green solid, black dashed, and red dot-dashed lines are the region boundaries for  $A_{32} = 2, \underline{4}, 15,$  and  $100$  Hz, respectively. VL; vertical line. DL; diagonal line. The purple diamond represents the parameter used in the simulation of Fig. 5 (a). The orange circle represents the actual experimental parameter.

(VL) at  $10^2$  Hz shifts to  $10$  or  $10^3$  Hz. In the next section, we examine the validity of the periodic/non-periodic classification discussed above using simulation.

## E. Numerical simulation

### 1. Results of the numerical simulation

In this section, we present numerically integrated solutions of the X2MB equations, actually the dimensionless version Eqs. (A2) - (A6), solved by the Runge-Kutta-fourth-order method. We first show a typical solution both inside and outside the periodic SR regions. We then give a brief summary of our numerical simulation studies.

*a. Inside the periodic SR region* As an example, we arbitrarily pick up a parameter set  $(P_{13}, A_{21}, A_{31}, A_{32}, \gamma_{32}) = (10^4, 10^3, \underline{10^2}, \underline{4}, \underline{10^7})$  Hz within the periodic SR region. It is represented by the purple diamond in Fig. 4. The simulation is started at  $t = 0$  with the initial populations  $\rho_{11}$ ,  $\rho_{22}$ , and  $\rho_{33}$  determined from the Boltzmann distribution at 4 K. The pulses begin to appear right after  $t = 0$ , and the peak interval and pulse shape gradually change until about

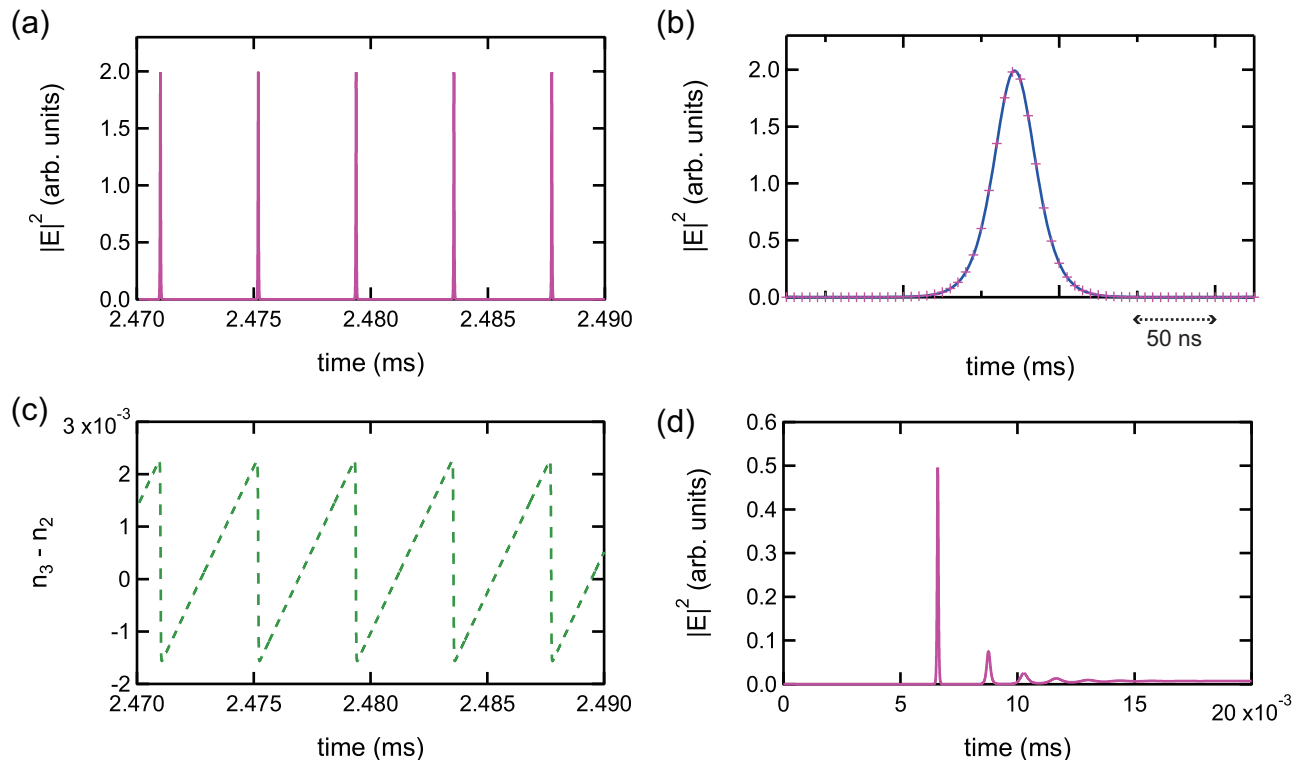


FIG. 5. (a) Example of a numerical simulation result within the periodic SR region. The parameters are  $(P_{13}, A_{21}, A_{31}, A_{32}, \gamma_{32}) = (10^4, 10^3, \underline{10^2}, \underline{4}, \underline{10^7})$  Hz. The magenta line is the square of the absolute value of the electric field, which is proportional to the instantaneous light intensity due to the emitted photons. (b) Extended view around a single SR pulse. The magenta crosses are the simulation results. The blue line is the fit by a sech-squared function. (c) Time evolution of the population inversion. (d) Example of a numerical simulation result outside the periodic SR region. The parameters are  $(P_{13}, A_{21}, A_{31}, A_{32}, \gamma_{32}) = (\underline{200}, \underline{2.5 \times 10^6}, \underline{10^2}, \underline{4}, \underline{10^7})$  Hz, which are the actual experimental parameters.

$t = 0.5$  ms, after which they remain constant, in other words, the optical pulses of the identical shape are generated at the constant interval. Figure 5 (a) shows the square of the electric field, or the instantaneous light intensity due to the emitted photons. The optical pulses are generated periodically. One of the pulses is shown in Fig. 5 (b). The magenta crosses are the simulation output. The FWHM pulse duration is  $\mathcal{O}(10)$  ns, which is  $10^6$  times shorter than the lifetime of the higher state of this transition (10 ms). The short pulse duration is one of the characteristics of SR. The blue line is the fit by a sech-squared function, which is another characteristics of SR when the macroscopic polarization (coherence) develops homogeneously over the target [14]. Figure 5 (c) is the population inversion between  $|2\rangle$  and  $|3\rangle$ . The population inversion increases linearly due to the pumping and the various decay processes, and decreases suddenly when the SR pulses are generated. The number of photons emitted in a single SR pulse is proportional to the sudden decrease of the population inversion. The periodic SR occurs as expected. Similar periodic behavior can be reproduced for other parameters within the periodic SR region.

*b. Outside the periodic SR region* Outside the periodic SR region, we pick up the parameter set  $(P_{13}, A_{21}, A_{31}, A_{32}, \gamma_{32}) = (\underline{200}, \underline{2.5 \times 10^6}, \underline{10^2}, \underline{4}, \underline{10^7})$  Hz. It corresponds to the actual experimental parameters represented by the orange circle in Fig. 4. The initial populations are the same as above. Figure 5 (d) shows the instantaneous light intensity due to the emitted photons. Several optical pulses are generated, but they decay within 10  $\mu$ s after the start of the pumping. The system reaches equilibrium, and the variables such as population, coherence, and electric field are almost constant. Thus, the periodic SR is no longer observable. This behavior is consistent with our expectation in Sec. III D. Similar decays are observed for other parameters outside the periodic SR region.

## 2. Brief summary of numerical simulation

As shown above, we performed the numerical simulation of the X2MB model by selecting one point each from inside and outside the periodic SR region. As expected from the analysis of the eigenvalues of the linearized X2MB equation, the periodic SR is reproduced

inside the periodic SR region and the SR pulses decay outside the region. Furthermore, we confirmed that this conclusion holds for at least 20 other points within each region. Near the boundary, however, the behavior of the numerical simulation does not exactly match the result of the eigenvalue analysis; roughly speaking, the boundary is blurred over a width of  $\sim A_{21}/4$ .

### F. Summary of the extended two-level model

In this section, we have constructed a model to reproduce the observed periodic SRs. The model, X2MB, is based on the Maxwell-Bloch equations with the reduced number of energy levels, and can be solved by numerical integrations. We first derived the T2B model from X2MB. It is at least partially integrable and gives analytical expressions for the SR period  $T$ , pulse duration  $\Delta T$  and the number of SR photons. These predictions are found to be in good agreement with the numerical simulation results of the X2MB model (see Appendix B). It is also found that the X2MB results show periodic SRs for a certain parameter region. By analyzing the eigenvalues of the linearized X2MB equations, we were able to successfully identify the parameter space where periodic SRs occur. Detailed numerical simulations support the validity of the eigenvalue analysis.

The important question here is whether the model as a whole can reproduce our experimental results. As already mentioned, the result of the simulation with the actual experimental parameters does not show any periodicity. In other words, the experimentally realized periodic SR is outside the theoretically predicted periodic SR region. This conclusion holds even if we consider the uncertainties of the parameters. The above conclusion implies that some other mechanism is needed to reproduce the observed periodic SR for the actual experimental parameter set.

## IV. OTHER POSSIBLE MECHANISMS FOR PERIODIC SR

In this section, we present other possible mechanisms that may explain the experimental results. So far, we have treated the parameters in X2MB as constants in time in a single simulation run. In the following, we assume that the parameters may vary dynamically due to certain nonlinear effects. For example, the decoherence rate  $\gamma_{32}$  and the decay rates  $A_{31}$  and  $A_{21}$ , associated with phonon decay processes, may vary due to the local increase in crystal temperature caused by the electric field generated. Recalling the optical Kerr effect, where the refractive index varies with the electric field intensity, the field decay rate  $\kappa$  may also vary due to the electric field. As an examples, we modulate  $\kappa$  as a function of the SR electric field. The intensity-dependent loss rate

was also discussed in the previous study on self-pulsing [19].

### A. Field decay rate modulation

We assume that the field decay rate  $\kappa$  in Eq. (6) decreases for the strong SR electric field. For simplicity, we binarize  $\kappa$  with respect to the threshold electric field as follows.

$$\kappa(E_0) = \begin{cases} \kappa_0 & (|E_0| < E_{\text{th}}) \\ \kappa_0/q & (|E_0| > E_{\text{th}}), \end{cases} \quad (19)$$

where  $E_0$  is the slowly varying envelope of the SR electric field,  $\kappa_0 = c/n_0L$  is the original field decay rate, and  $E_{\text{th}}$  is the electric field threshold. The quantity  $q$  ( $q > 1$ ) defines how much  $\kappa$  decreases. In the following, we will refer to  $(q, E_{\text{th}})$  as the modulation parameters. A possible mechanism of  $\kappa$  modulation, the reduction of  $\kappa$  due to the cavity effect in the crystal, is shown in Appendix C.

When the modulation of  $\kappa$  is introduced, the periodic SR can occur even under the actual parameter set  $(P_{13}, A_{21}, A_{31}, A_{32}, \gamma_{32}) = (200, 2.5 \times 10^6, 10^2, 4, 10^7)$  Hz. In this case, coherence and the electric field increase slowly at first. Then, when  $|E_0|$  exceeds the threshold  $E_{\text{th}}$ , coherence develops faster than without modulation due to the reduced  $\kappa$ . In effect, SR pulses are emitted more easily for a broader parameter space. To find the best parameter set, we use the following search strategy. First, we vary the actual parameters within the uncertainty range shown in Table I with the fixed modulation parameters  $(q, E_{\text{th}})$ . We then vary  $q$  while keeping  $E_{\text{th}}$  fixed to see if we can achieve the experimental result. The process is repeated many times (so the study is of a trial-and-error nature). We found that the best result gives

$$(T, \Delta T, N_{\text{SR}}) = (45 \mu\text{s}, 14 \text{ ns}, 8.5 \times 10^{12}), \quad (20)$$

with the parameter set of  $(P_{13}, A_{21}, A_{31}, A_{32}, \gamma_{32}) = (100, 2.5 \times 10^6, 110, 2, 10^8)$  and  $(q, E_{\text{th}}) = (2, 10^{-5} \times (\hbar\Omega_0/d_{32}))$ . Figure 6 (a) shows the resulting SR pulses from the numerical simulation. Eq. (20) should be compared with Eq. (1), the observed values: our simulation results deviate from the actual ones by a factor of  $\sim 4$ . We note that the above simulations are rather insensitive to  $E_{\text{th}}$  as long as  $E_{\text{th}} < 10^{-4} \times (\hbar\Omega_0/d_{32})$ . We also note that if we allow  $P_{13}$  to vary outside the uncertainty range, we can obtain a much more satisfactory result;  $(T, \Delta T, N_{\text{SR}}) = (137 \mu\text{s}, 16 \text{ ns}, 7.7 \times 10^{12})$ , which is realized with the parameter set  $(P_{13}, A_{21}, A_{31}, A_{32}, \gamma_{32}) = (30, 2.5 \times 10^6, 110, 2, 10^8)$  Hz and  $(q, E_{\text{th}}) = (2, 10^{-5} \times (\hbar\Omega_0/d_{32}))$ .

Figure 6 (b) shows the dependence of the period on  $q$ . The longer period can be seen for the higher  $q$ . The actual value of  $q$  is not clear and should be determined

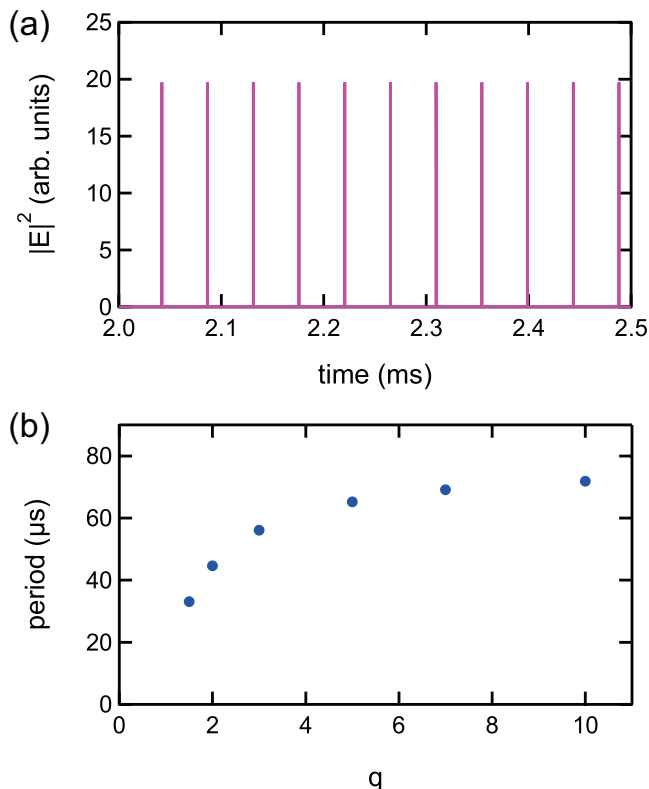


FIG. 6. (a) Result of a numerical simulation with  $\kappa$  modulation. The magenta line is the square of the absolute value of the electric field. The parameters are  $(P_{13}, A_{21}, A_{31}, A_{32}, \gamma_{32}) = (100, 2.5 \times 10^6, 110, 2, 10^8)$  Hz and  $(q, E_{\text{th}}) = (2, 10^{-5} \times (\hbar\Omega_0/d_{32}))$ . (b) Dependence of the period on  $q$  in Eq. (19).

by experiments. Whether or not the  $\kappa$  modulation is realized in our actual experiment also remains unanswered in this study. We may be able to prove/disprove the proposed mechanism by an experiment, for example, with a crystal having non-parallel exit/entry surfaces or surfaces with an appropriate anti-reflection coating. Such an experiment is also left as a future task.

## V. SUMMARY

In this paper, we have performed theoretical and simulation studies to investigate the periodic superradiance observed in an Er:YSO crystal [10]. Our particular motivation is to understand the phenomena more quantitatively. In particular, we want to reproduce by simulation the characteristic SR quantities such as the period  $T$ , the pulse duration  $\Delta T$ , and the SR photon number  $N_{\text{SR}}$ . See Eq. (1) for the experimental values. For this purpose, we first constructed a model based on the Maxwell-Bloch equations. This model, X2MB, has a reduced number of energy levels, *i.e.* a pair of the SR states and a reservoir, and is solved by numerical simulation in this study. It is

found that the model successfully generates periodic SR pulses under continuous laser excitation.

We then derived a simpler model from X2MB. This model, T2B, is actually a set of nonlinear differential equations with only two variables, the coherence and the population differences between the two SR states. A nice feature of the model is that it has an integral: indeed, the SR characteristic quantities  $(T, \Delta T, N_{\text{SR}})$  can be expressed analytically with an integral. It is found that the prediction by the analytical expressions and the numerical results by X2MB simulations are in good agreement. It is clear that this model contains essential features of the periodic SR.

The original X2MB model has many parameters, and it exhibits periodic SRs for a certain limited region of the parameter space. It is found possible to classify the parameter space into two distinct regions, the periodic and non-periodic regions, for a given set of parameters. The classification is made by analyzing the eigenvalues of the linearized X2MB equations around the equilibrium points, and is confirmed to be valid by the X2MB numerical simulations.

Having established the analysis tool mentioned above, we investigated whether or not periodic SR can be realized under the actual experimental conditions. We found that our experimental parameter set is outside the periodic SR region, and that this conclusion holds even when we allow the parameters to vary over a wide range of uncertainties. We conclude that some other mechanism(s) is required to reproduce the observed periodic SR.

As an example of such mechanisms, we presented a modulation of the field decay constant  $\kappa$ , *i.e.* the electric field emission rate to the outside of the crystal, as a function of the electric field strength. It is found that the X2MB model with this modification exhibits periodic SR even for the actual parameter set. With some parameter adjustments within the uncertainties, the best simulation results of  $(T, \Delta T, N_{\text{SR}})$  turn out to be off by a factor 4 from the experimental values. See Eq.(20). We conclude that the X2MB model with this modification gives much more satisfactory results. Whether or not the  $\kappa$  modulation is realized in our actual experiment remains unanswered in this study, and its experimental verification/refutation is left as a future task.

The periodic SR is an interesting phenomenon because it seems to be in sharp contrast to the stochastic nature of SR. The study presented in this paper contributes to deeper understanding of the new properties of the SR, in particular, it reveals the mathematical structures behind this phenomenon. The study is also important for the application of the phenomenon to other systems. If the level system is found in real atomic or ionic systems that satisfies the necessary condition for the periodic SR, it would be possible to predict and prepare a system that emits periodic optical pulses in response to a CW input without any complex mechanisms such as modulation of the field decay rate. This system has a potential as a light source, where coherent optical pulses are periodi-

cally generated in a simple system without Q-switching.

We believe that the above studies explore intriguing aspects of the Maxwell-Bloch equations and shed new light on SR physics.

### ACKNOWLEDGMENTS

We thank professor K. An for helpful discussions and warm encouragement. This work was supported by JSPS KAKENHI (Grants No. JP19H00686, No. JP20H00161, and No. JP21H01112) and the Korea Research Foundation (Grant No. 2020R1A2C3009299).

### Appendix A: Derivation of equations

In the main text of this paper, we introduced the T2B model, Eqs. (10) - (11). Here we derive these equations from the X2MB equations, Eqs. (2) - (6).

First, to make the equations dimensionless, we introduce

$$\epsilon_{\text{SR}} \equiv \frac{\Omega_s}{\Omega_0}, \quad \tilde{t} \equiv t\Omega_0. \quad (\text{A1})$$

As mentioned in the main text, we set  $\Omega_s$  and  $\rho_{32}$  as real numbers without loss of generality. Thus  $\epsilon_{\text{SR}}$  is a real number. The dimensionless Maxwell-Bloch equations are given by

$$\frac{d\rho_{11}}{d\tilde{t}} = -p_{13}\rho_{11} + a_{31}\rho_{33} + a_{21}\rho_{22}, \quad (\text{A2})$$

$$\frac{d\rho_{22}}{d\tilde{t}} = \epsilon_{\text{SR}}\rho_{32} + a_{32}\rho_{33} - a_{21}\rho_{22}, \quad (\text{A3})$$

$$\frac{d\rho_{33}}{d\tilde{t}} = -\epsilon_{\text{SR}}\rho_{32} + p_{13}\rho_{11} - (a_{31} + a_{32})\rho_{33}, \quad (\text{A4})$$

$$\frac{d\rho_{32}}{d\tilde{t}} = \frac{\epsilon_{\text{SR}}}{2}(\rho_{33} - \rho_{22}) - \tilde{\gamma}_{32}\rho_{32}, \quad (\text{A5})$$

$$\frac{\partial \epsilon_{\text{SR}}}{\partial \tilde{t}} = -\tilde{\kappa}\epsilon_{\text{SR}} + \rho_{32} + R_{\text{sp}}\rho_{33}, \quad (\text{A6})$$

where  $p_{13} = P_{13}/\Omega_0$ ,  $a_{ij} = A_{ij}/\Omega_0$ ,  $\tilde{\gamma}_{32} = \gamma_{32}/\Omega_0$ , and  $\tilde{\kappa} = \kappa/\Omega_0$ .

Introducing the new variables

$$u_0 \equiv \epsilon_{\text{SR}}, \quad u_1 \equiv \rho_{32}, \quad (\text{A7})$$

$$u_2 \equiv \frac{\rho_{33} - \rho_{22}}{2}, \quad u_3 \equiv \frac{\rho_{33} + \rho_{22}}{2}, \quad (\text{A8})$$

and using the relation  $\rho_{11} + \rho_{22} + \rho_{33} = 1$ , Eqs. (A2) - (A6) are reduced as follows.

$$\frac{du_0}{d\tilde{t}} = -b_{00}u_0 + u_1, \quad (\text{A9})$$

$$\frac{du_1}{d\tilde{t}} = u_0u_2 - b_{11}u_1, \quad (\text{A10})$$

$$\frac{du_2}{d\tilde{t}} = -u_0u_1 + b_{20} + b_{22}u_2 + b_{23}u_3, \quad (\text{A11})$$

$$\frac{du_3}{d\tilde{t}} = b_{30} + b_{32}u_2 + b_{33}u_3, \quad (\text{A12})$$

where

$$b_{00} \equiv \tilde{\kappa}, \quad b_{11} \equiv \tilde{\gamma}_{32}, \quad (\text{A13})$$

$$b_{20} \equiv \frac{p_{13}}{2}, \quad b_{22} \equiv \frac{-a_{31} - a_{21} - 2a_{32}}{2}, \quad (\text{A14})$$

$$b_{23} \equiv \frac{-2p_{13} - a_{31} + a_{21} - 2a_{32}}{2}, \quad b_{30} \equiv \frac{p_{13}}{2}, \quad (\text{A15})$$

$$b_{32} \equiv \frac{-a_{31} + a_{21}}{2}, \quad b_{33} \equiv \frac{-2p_{13} - a_{31} - a_{21}}{2}. \quad (\text{A16})$$

The coherence trigger term in Eq. (A6) is ignored here. When the time derivatives in Eqs. (A9) - (A12) are set to zero,  $u_i$  at the equilibrium point are given by

$$u_0^e = b_{00}^{-1}u_1^e, \quad (\text{A17})$$

$$u_1^e = \pm \sqrt{b_{00} \left( b_{20} + b_{00}b_{11}b_{22} - \frac{b_{23}}{b_{33}}(b_{30} + b_{00}b_{11}b_{32}) \right)}, \quad (\text{A18})$$

$$u_2^e = b_{00}b_{11}, \quad (\text{A19})$$

$$u_3^e = -\frac{b_{30} + b_{00}b_{11}b_{32}}{b_{33}}. \quad (\text{A20})$$

There is also the following trivial solution.

$$u_0^{e,\text{triv}} = u_1^{e,\text{triv}} = 0, \quad (\text{A21})$$

$$u_2^{e,\text{triv}} = -\frac{b_{33}b_{20} - b_{23}b_{30}}{b_{22}b_{33} - b_{23}b_{32}}, \quad (\text{A22})$$

$$u_3^{e,\text{triv}} = \frac{b_{32}b_{20} - b_{22}b_{30}}{b_{22}b_{33} - b_{23}b_{32}}. \quad (\text{A23})$$

In Eq. (A9), the time derivative of  $u_0$  can be ignored because  $b_{00}$ , which corresponds to the field decay rate  $\kappa$ , is very high and dominates the time evolution of the system. Using this approximation,  $u_0 = b_{00}^{-1}u_1$ , the electric field is proportional to the coherence. By introducing the following new variables

$$X \equiv \frac{u_1}{u_1^e}, \quad Y \equiv \frac{u_2 - u_2^e}{u_1^e}, \quad \tau \equiv \frac{u_1^e \tilde{t}}{b_{00}}, \quad (\text{A24})$$

Eq. (A10) is reduced to

$$\frac{dX}{d\tau} = XY. \quad (\text{A25})$$

While  $u_0$  and  $u_1$  vary by many orders of magnitude around the equilibrium point, the variations of  $u_2$  and  $u_3$  are very small compared to the equilibrium point values of  $u_2^e$  and  $u_3^e$ . In Eqs. (A11) and (A12), we approximate  $u_2$  and  $u_3$  by replacing  $u_2^e$  and  $u_3^e$ . Thus, the following equations are obtained.

$$\frac{dY}{d\tau} = -(X^2 - 1), \quad (\text{A26})$$

$$\frac{du_3}{d\tau} = 0, \quad (\text{A27})$$

The T2B model, Eqs. (10) and (11), is derived by the above procedure. In addition,  $\rho_{11} (= 1 - 2u_3)$  is constant in this model.

## Appendix B: Comparison of the analytical solution of the T2B model and numerical simulation of the X2MB model

To confirm the validity of the T2B model Eqs. (10) - (11) derived with several approximations, we compare the analytical solution of the T2B model and the numerical simulation result of the X2MB model for the same parameter set. We vary  $A_{21}$  in the periodic SR region while keeping the other parameters fixed. In the numerical simulation, we take the values after the period and pulse shape have become constant. As a point of caution, the analytical solution requires the prediction of the integration constant  $C$ . We use the maximum value of coherence  $\rho_{\max}$  in the numerical simulation to find  $C$ . Therefore, one numerical simulation is necessary to obtain one analytical solution. With  $C$  above, the period, FWHM pulse duration, and SR photon number are obtained.

The left column of Fig. 7 shows (a) period, (b) FWHM pulse duration, and (c) SR photon number for the different decay rates  $A_{21}$  under  $(P_{13}, A_{31}, A_{32}, \gamma_{32}) = (10^4, \underline{10^2}, \underline{4}, \underline{10^7})$  Hz. This corresponds to the variation on the horizontal line  $P_{13} = 10^4$  Hz in the green region of Fig. 4. The right column of Fig. 7 shows the results for the decay rate  $A_{21}$  under  $(P_{13}, A_{31}, A_{32}, \gamma_{32}) = (\underline{200}, \underline{10^2}, 100, \underline{10^7})$  Hz. This corresponds to the variation on the horizontal line  $P_{13} = 200$  Hz in the red region of Fig. 4. The blue crosses and red circles represent the results of the analytical solution of the T2B model and the numerical simulation of the X2MB model, respectively. They are in good agreement. This result shows the validity of several approximations used in the T2B model. The FWHM pulse duration,  $\mathcal{O}(10)$  ns, and the SR photon number,  $\mathcal{O}(10^{12\pm 1})$ , are comparable with those in the experimental data. The period,  $\mathcal{O}(1)$   $\mu$ s, is two orders of magnitude shorter than that in the experiment. As  $A_{21}$  increases, the period becomes shorter. This is because as  $A_{21}$  increases, the population inversion reaches the threshold of SR earlier. On the other hand, as  $A_{21}$  increases, the FWHM pulse duration becomes shorter and the number of SR photons increases. The FWHM pulse duration is inversely proportional to the SR photon number, which is one of the characteristics of SR.

## Appendix C: Possible mechanism of field decay constant modulation

In Sec. IV, we perform the numerical simulation assuming that the field decay rate  $\kappa$  varies as a function of the electric field. A possible mechanism for dynamically varying  $\kappa$  is presented here.

## 1. Principle

### a. Formation of refractive index modulation

The population of  $|3\rangle$  in Fig. 2 is gradually increased by the pumping  $P_{13}$ . The excited  $\text{Er}^{3+}$  ions deexcite to  $|2\rangle$  with photons, which generate an electric field. The reflection of the electric field at the two crystal surfaces creates a very low finesse cavity. The surface reflection, estimated from the refractive index, is 8 %. A small standing wave is formed and the electric field intensity is periodically modulated. At the anti-nodes the population of  $|3\rangle$  decreases faster than at the nodes due to the higher stimulated emission rate. The electric field at the anti-nodes is further increased. The refractive index of the crystal  $n$  changes in response to an electric field due to the optical Kerr effect.

$$n = n_0 + 2\tilde{n}_2|E|^2, \quad (\text{C1})$$

where  $E$  is the electric field,  $n_0$  is the refractive index in the low-intensity limit, and  $\tilde{n}_2$  is the optical Kerr coefficient. Therefore, the refractive index modulation is generated.

### b. Decrease in field decay rate due to increased finesse

For simplicity, we assume a medium whose refractive index has two values of  $n_H$  and  $n_L$ , which change periodically with a period of  $d$  along the  $z$ -axis, as shown in Fig. 8 (a). We define the mean and difference index as

$$\bar{n} = \frac{n_H + n_L}{2}, \quad \Delta n = \frac{n_H - n_L}{2}. \quad (\text{C2})$$

The wavelength of the electromagnetic wave propagating in the medium is  $\lambda_0 = 4\bar{n}d$  when measured in vacuum. The transfer matrix [20] for the region  $j$  ( $j = H, L$ ) is given by

$$\mathcal{M}_j(\Delta z) \equiv \begin{pmatrix} \cos(k_j \Delta z) & \frac{i}{n_j} \sin(k_j \Delta z) \\ in_j \sin(k_j \Delta z) & \cos(k_j \Delta z) \end{pmatrix}, \quad (\text{C3})$$

$$\begin{pmatrix} E(z + \Delta z) \\ cB(z + \Delta z) \end{pmatrix} = \mathcal{M}_j(\Delta z) \begin{pmatrix} E(\Delta z) \\ cB(\Delta z) \end{pmatrix}, \quad (\text{C4})$$

where  $k_j = n_j k_0$  is the wave vector of the photon traveling through the crystal. Now we look at the multilayer structure again. If we denote the input and output fields by  $E_{\text{in}}, cB_{\text{in}}$  and  $E_{\text{out}}, cB_{\text{out}}$ , respectively, they are connected by the following relationship.

$$\begin{pmatrix} E_{\text{in}} \\ cB_{\text{in}} \end{pmatrix} = (\mathcal{M}_H(d)\mathcal{M}_L(d))^{-N_p} \begin{pmatrix} E_{\text{out}} \\ cB_{\text{out}} \end{pmatrix}. \quad (\text{C5})$$

The number of the index pairs  $N_p$  can be roughly estimated as

$$N_p = \frac{\bar{n}L}{\lambda_0/2} \sim 10^4, \quad (\text{C6})$$

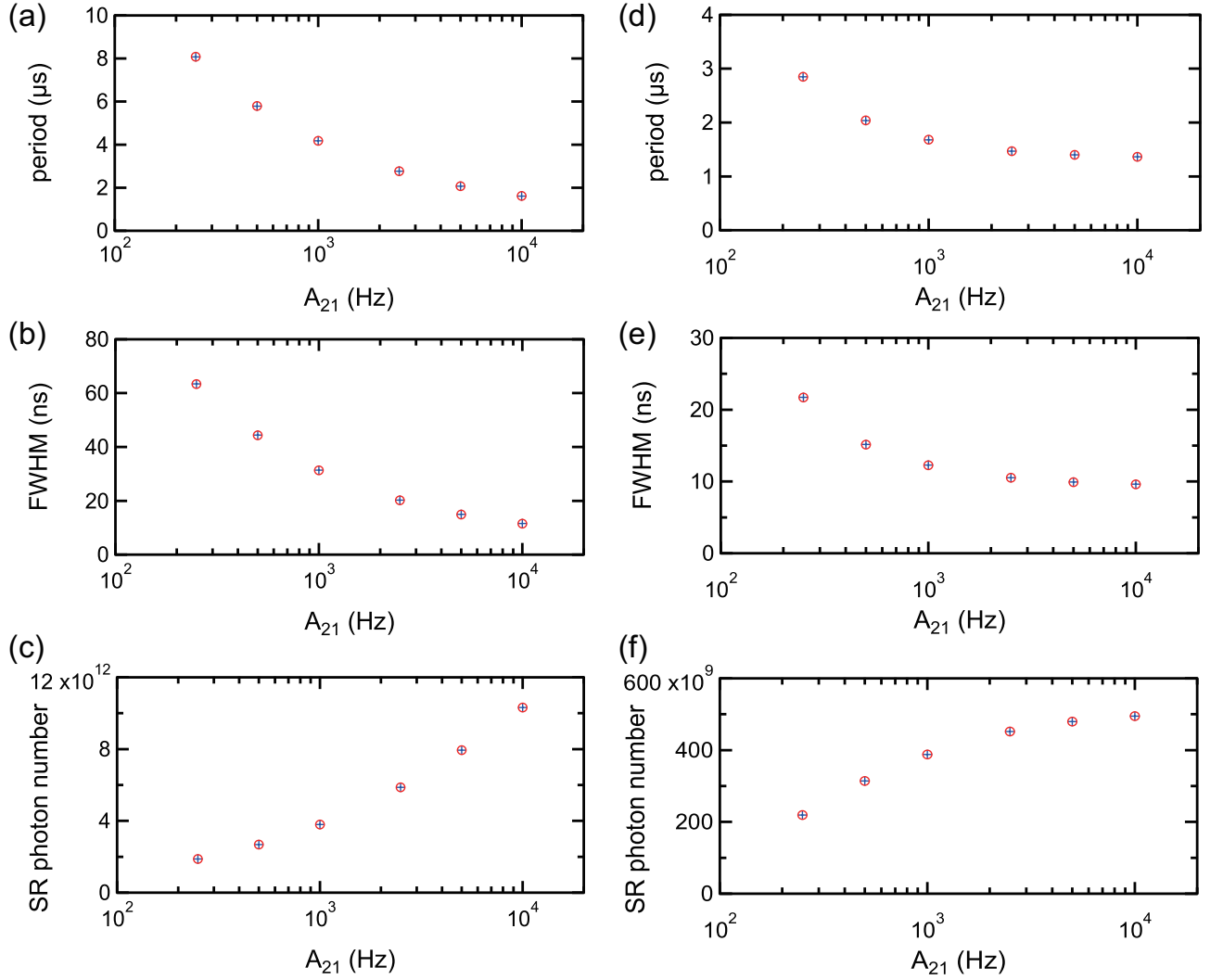


FIG. 7. Comparison of the analytical solution of the T2B model and the numerical simulation of the X2MB model. The left column shows (a) period, (b) FWHM pulse duration, (c) SR photon number for the different decay rates  $A_{21}$  under  $(P_{13}, A_{31}, A_{32}, \gamma_{32}) = (10^4, 10^2, 4, 10^7)$  Hz. The right column shows (d) period, (e) FWHM pulse duration, (f) SR photon number for the decay rate  $A_{21}$  under  $(P_{13}, A_{31}, A_{32}, \gamma_{32}) = (200, 10^2, 100, 10^7)$  Hz. The blue crosses and red circles represent the results of the analytical solution and the numerical simulation, respectively.

for the mean refractive index  $\bar{n} = 1.8$ , the target length  $L = 6$  mm, and the wavelength of SR  $\lambda_0 = 1.545$   $\mu$ m. If the incident beam is injected from the left, then there are both right-moving (injected) and left-moving (reflected) beams at the input boundary, but there is no left-moving field at the output boundary. Denoting the incident field by  $E_1$ , the reflected field by  $E_R$ , and the transmitted field by  $E_T$ , we have

$$E_{\text{in}} = E_1 + E_R, \quad cB_{\text{in}} = E_1 - E_R, \quad (\text{C7})$$

$$E_{\text{out}} = E_T, \quad cB_{\text{out}} = E_T. \quad (\text{C8})$$

Denoting the matrix elements of  $(\mathcal{M}_H \mathcal{M}_L)^{-N_p}$  by  $m_{ij}$ , we obtain the complex reflectivity  $r$  as

$$r \equiv \frac{E_R}{E_1} = \frac{(m_{11} + m_{12}) - (m_{21} + m_{22})}{(m_{11} + m_{12}) + (m_{21} + m_{22})}. \quad (\text{C9})$$

Figure 8 (b) shows  $R (= |r|^2)$  as a function of  $\Delta n$ . There seems to be a threshold around  $\Delta n \sim 1 \times 10^{-4}$ , above which  $R$  is close to 1. Therefore, the finesse of the crystal  $F = \pi\sqrt{R}/(1-R)$  increases rapidly. This is a highly non-linear effect. The time it takes for the generated electric field to be emitted from the target increases by a factor of  $\sim F$ . Then the field decay rate  $\kappa$  decreases by a factor of  $\sim F$ . This is the possible mechanism by which the field decay rate  $\kappa$  varies as a function of the electric field. For the strong electric field, the refractive index variation  $\Delta n$  increases and the field decay rate  $\kappa$  decreases significantly.

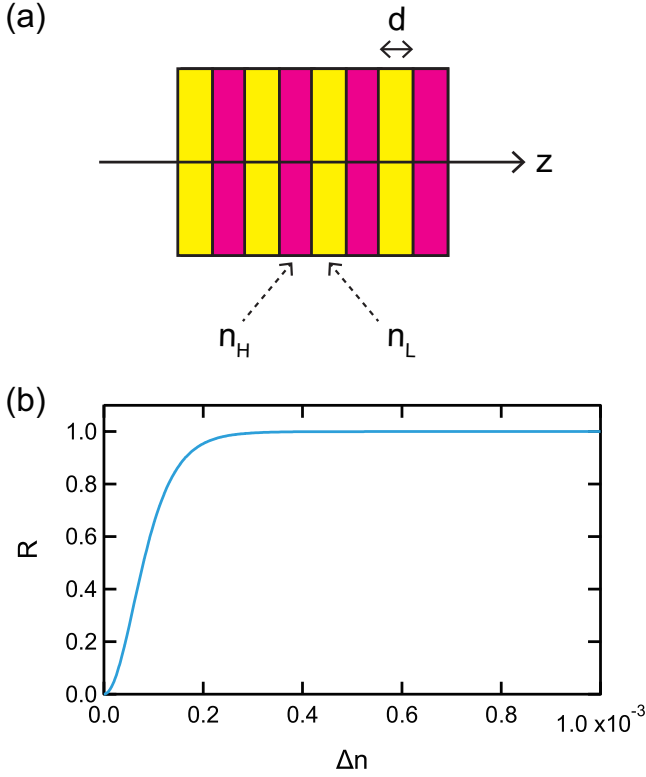


FIG. 8. (a) Multilayer structure whose refractive index has two values of  $n_H$  and  $n_L$ , changing periodically with a period of  $d$  along the  $z$ -axis. (b) Dependence of the reflectance  $R$  on the refractive index variation  $\Delta n$ .

## 2. Refractive index variation $\Delta n$

We estimate the refractive index variation  $\Delta n$  for a given electric field  $E_{SR}$ . According to the results of Ref. [21], in particular Eq.(6.3.28) [22], the electric susceptibility  $\chi_e$  is given by

$$\chi_e = \frac{-\alpha_0(0)}{\omega_{32}/c} \frac{\delta T_2 - i}{1 + (\delta T_2)^2 + |E|^2/|E_S^0|^2}, \quad (C10)$$

$$|E_S^0|^2 = \frac{\hbar^2}{4|d_{32}|^2 T_1 T_2}, \quad (C11)$$

$$\alpha_0(0) = -\frac{\omega_{32}}{c} \left[ N_0(\rho_{33} - \rho_{22}) |d_{32}|^2 \frac{T_2}{\epsilon_0 \hbar} \right], \quad (C12)$$

where  $\alpha_0(0)$  is the absorption coefficient at zero detuning,  $N_0$  is the number density of  $\text{Er}^{3+}$  ions at site 2,  $\rho_{ij}$  is

the density matrix element,  $d_{32}$  is the dipole moment,  $\delta$  is the detuning,  $T_1$  is the lifetime of  $|3\rangle$ , and  $T_2$  is the decoherence time. The third-order susceptibility  $\chi_e^{(3)}$  has the relation  $\tilde{n}_2 = 3\chi_e^{(3)}/4n_0$  with  $\tilde{n}_2$ . Expanding Eq. (C10) with respect to  $|E|/|E_S^0|$ , the third-order susceptibility  $\chi_e^{(3)}$  is

$$\chi_e^{(3)} = \frac{\alpha_0(0)}{3\omega_{32}/c} \frac{\delta T_2}{[1 + (\delta T_2)^2]^2} \frac{1}{|E_S^0|^2}. \quad (C13)$$

The number density of  $\text{Er}^{3+}$  ions relevant to the index variation  $\Delta n$  is given by the SR electric field  $E_{SR}$ . The number density can be replaced by

$$N_0(\rho_{33} - \rho_{22}) \sim \frac{\epsilon_0 n_0^2 |E_{SR}|^2}{\hbar \omega_{32}}. \quad (C14)$$

With this substitution, the refractive index variation  $\Delta n$  is estimated by

$$\begin{aligned} \Delta n &\sim 2 \times \frac{3}{4n_0} |\Delta \chi_e^{(3)}| \times |E_{SR}|^2 \\ &\sim \left[ \frac{\epsilon_0 n_0 |E_{SR}|^2}{2\hbar \omega_{32}} |d_{32}|^2 \frac{T_2}{\epsilon_0 \hbar} \right] \frac{\delta T_2}{[1 + (\delta T_2)^2]^2} \frac{|E_{SR}|^2}{|E_S^0|^2}. \end{aligned} \quad (C15)$$

To estimate  $\Delta n$ , we need to know several parameters, of which  $\delta$  and  $E_{SR}$  are the least well known. Naively  $\delta$  is expected to be smaller than the width of the  $\text{Er}^{3+}$  ion ensemble, *i.e.*  $\delta < 10^9$  Hz. Remembering that  $\Delta n \sim 10^{-4}$  is the threshold for the sharp increase in  $R$  or the sharp decrease in  $\kappa$ , we evaluate  $E_{SR}$  that gives  $\Delta n = 10^{-4}$ . It turns out that

$$|E_{SR}| \sim 6 \times 10^5 \text{ V/m}, \quad (C17)$$

for  $\delta = 10^9$  Hz. The number of photons giving this electric field is estimated to be

$$\frac{\epsilon_0 n_0^2 |E_{SR}|^2}{\hbar \omega_{32}} \times \pi w_0^2 \times \frac{c}{n_0} \times \Delta T \sim 1 \times 10^{13}. \quad (C18)$$

$\Delta T$  is the duration of the SR pulse and is here set to  $10^{-8}$  s. On the other hand, the electric field estimated from the measured SR pulses is  $\sim 2 \times 10^5$  V/m. We note that if we assume  $\delta = 10^8$  Hz, then we find  $|E_{SR}| \sim 1 \times 10^5$  V/m and the corresponding photon number  $\sim 3 \times 10^{11}$ , much smaller than those of Eqs.(C17) and (C18). These considerations suggest that the modulation of the field decay rate  $\kappa$  may occur.

[1] R. H. Dicke, Coherence in Spontaneous Radiation Processes, Phys. Rev. **93**, 99 (1954).

[2] N. Skribanowitz, I. P. Herman, J. C. MacGillivray, and M. S. Feld, Observation of Dicke Superradiance in Optically Pumped HF Gas, Phys. Rev. Lett. **30**, 309 (1973).

[3] M. Gross, C. Fabre, P. Pillet, and S. Haroche, Observation of Near-Infrared Dicke Superradiance on Cascading Transitions in Atomic Sodium, Phys. Rev. Lett. **36**, 1035 (1976).

- [4] N. Carlson, D. Jackson, A. Schawlow, M. Gross, and S. Haroche, Superradiance triggering spectroscopy, *Optics Communications* **32**, 350 (1980).
- [5] R. Florian, L. Schwan, and D. Schmid, Superradiance and high-gain mirrorless laser activity of  $O^{-}_2$ -centers in KCl, *Solid State Communications* **42**, 55 (1982).
- [6] G. Rainò, M. A. Becker, M. I. Bodnarchuk, R. F. Mahrt, M. V. Kovalenko, and T. Stöferle, Superfluorescence from lead halide perovskite quantum dot superlattices, *Nature* **563**, 671 (2018).
- [7] A. Angerer, K. Streltsov, T. Astner, S. Putz, H. Sumiya, S. Onoda, J. Isoya, W. J. Munro, K. Nemoto, J. Schmiedmayer, and J. Majer, Superradiant emission from colour centres in diamond, *Nature Physics* **14**, 1168 (2018).
- [8] C. Braggio, F. Chioffi, G. Carugno, A. Ortolan, and G. Ruoso, Spontaneous formation of a macroscopically extended coherent state, *Phys. Rev. Research* **2**, 033059 (2020).
- [9] K. Cong, Q. Zhang, Y. Wang, G. T. Noe, A. Belyanin, and J. Kono, Dicke superradiance in solids, *J. Opt. Soc. Am. B* **33**, C80 (2016).
- [10] H. Hara, J. Han, Y. Imai, N. Sasao, A. Yoshimi, K. Yoshimura, M. Yoshimura, and Y. Miyamoto, Periodic superradiance in an Er:YSO crystal, *Physical Review Research* **6**, 013005 (2024).
- [11] M. Benedict, A. Ermolaev, V. Malyshev, I. Sokolov, and E. Trifonov, *Super-radiance: Multiatomic Coherent Emission* (CRC Press, 1996).
- [12] F. Sanchez, P. L. Boudec, P.-L. François, and G. Stephan, Effects of ion pairs on the dynamics of erbium-doped fiber lasers, *Phys. Rev. A* **48**, 2220 (1993).
- [13] S. H. Strogatz, *Nonlinear Dynamics and Chaos: With Applications to Physics, Biology, Chemistry, and Engineering (Studies in Nonlinearity)* (2001).
- [14] R. Bonifacio and L. A. Lugiato, Cooperative radiation processes in two-level systems: Superfluorescence, *Phys. Rev. A* **11**, 1507 (1975).
- [15] R. M. Corless, G. H. Gonnet, D. E. Hare, D. J. Jeffrey, and D. E. Knuth, On the lambert  $W$  function, *Advances in Computational mathematics* **5**, 329 (1996).
- [16] L. Petersen, *High-resolution spectroscopy of praseodymium ions in a solid matrix: towards single-ion detection sensitivity*, Ph.D. thesis, ETH Zurich (2011).
- [17] N. Carvalho, J.-M. Le Floch, J. Krupka, and M. E. Tobar, Multi-mode technique for the determination of the biaxial  $Y_2SiO_5$  permittivity tensor from 300 to 6 K, *Applied Physics Letters* **106**, 192904 (2015).
- [18] T. Böttger, Y. Sun, C. W. Thiel, and R. L. Cone, Spectroscopy and dynamics of  $Er^{3+}:Y_2SiO_5$  at 1.5  $\mu m$ , *Phys. Rev. B* **74**, 075107 (2006).
- [19] J. Shang, T. Feng, S. Zhao, J. Zhao, Y. Zhao, Y. Song, and T. Li, An investigation into self-pulsing behavior in an Er-doped ring laser, *Applied Physics Express* **13**, 112006 (2020).
- [20] G. R. Fowles, *Introduction to Modern Optics* (Courier Corporation, 1989).
- [21] R. W. Boyd, *Nonlinear Optics, Third Edition*, 3rd ed. (Academic Press, Inc., USA, 2008).
- [22] It assumes a near-resonant, steady-state two-level system.